Velocity map imaging with non-uniform detection: quantitative molecular axis alignment measurements via Coulomb explosion imaging

Jonathan G. Underwood[a)] and I. Procino
Department of Physics and Astronomy, University College London, Gower Street, London WC1E 6BT, United Kingdom

L. Christiansen, J. Maurer, and H. Stapelfeldt
Department of Chemistry, University of Aarhus, DK-8000 Århus C, Denmark

(Dated: 9 July 2015)

We present a method for inverting charged particle velocity map images which incoorporates a non-uniform detection function. This method is applied to the specific case of extracting molecular axis alignment from Coulomb explosion imaging probes in which the probe itself has a dependence on molecular orientation which often removes cylindrical symmetry from the experiment and prevents the use of standard inversion techniques for the recovery of the molecular axis distribution. By incorporating the known detection function, it is possible to remove the angular bias of the Coulomb explosion probe process and invert the image to allow quantitative measurement of the degree of molecular axis alignment.

I. INTRODUCTION

Photofragment imaging has become a standard tool in the chemical physicists arsenal of tools for detailed measurements of processes in gas phase molecules[1–3] since its inception in the 1980s[4] and the subsequent evolution of the technique known as velocity map imaging (VMI).[5]

In a photofragment imaging experiment an expanding sphere of charged particles is projected onto a two-dimensional (2D) position sensitive detector. The aim of this detection method is to extract the original 3D distribution of the charged particles from the 2D projection, and so recover the energy and angular information regarding the fragmentation process. While it is possible to arrange to image only a central 2D slice of the 3D distribution using laser or electrostatic slicing techniques[3,6] it is frequently the case that experimental considerations require imaging of the 2D projection to regain the 3D distribution.[1,7–10] Reconstructing the 3D distribution from a single 2D projection requires that the experiment is cylindrically symmetric about an axis lying in the plane of the detector; if this condition is not met, then in general it is only possible to reconstruct the 3D distribution tomographically from multiple 2D projections.[11,12]

However, there exists another class of experiments in which the experiment lacks cylindrical symmetry due to a non-uniform detection function that is otherwise measurable or known. In these circumstances we show here that it is possible to invert a single 2D image to recover the 3D distribution while simultaneously correcting for the non-uniform detection function.

Our methodology is motivated by the desire to characterize the degree of molecular axis alignment and orientation produced through the interaction of a molecular sample with intense non-resonant laser fields.[13–19]

For such aligned/oriented samples to be useful for subsequent experiments, such as x-ray[20,21] or electron diffraction,[22–24] high-order harmonic generation,[25,26] and photodissociation or photoionization studies,[27–29] it is necessary to characterize and quantify the degree of alignment and orientation produced. It is common practice to utilize Coulomb explosion imaging (CEI) for this characterization[13–15,17–19] where an intense probe laser pulse with duration much shorter than molecular rotation is used to remove multiple electrons from the molecules under study. The multiply ionized molecules subsequently undergo rapid fragmentation due to Coulomb repulsion, and imaging the resulting ion fragments is then used to establish the orientation of the molecules prior to ionization; under the assumptions that the fragmentation happens rapidly with respect to rotation, and that the fragments recoil in the direction of molecular bonds, there is a direct correlation between the fragment recoil and the molecular orientation. While this technique has been very succesful at analysing alignment and orientation of molecular samples it has proved difficult to fully quantify the degree of alignment/orientation since the ionization process in CEI has a strong dependence on the molecular orientation with respect to the ionizing laser polarization. In fact it has become common practice to characterize the molecular axis alignment and orientation in such experiments using expectation values calculated for the resulting VMI image, such as $\langle \cos^2 \theta_{2D} \rangle$, where θ_{2D} is the angle in the plane of the detector measured from the axis of laser polarization. This expectation value includes anisotropy due to the CEI probing, and is calculated in lieu of a method suitable for extracting the true molecular axis distribution. Here we show that it is possible, under certain circumstances, to remove the effect of the orientation dependence of the CEI probe from the measured molecular axis distribution, and so extract the true moments of the axis distribution. This is possible by making an independent measurement of the CEI orientation dependence using an isotropic gas under the same conditions as the alignment measurement which
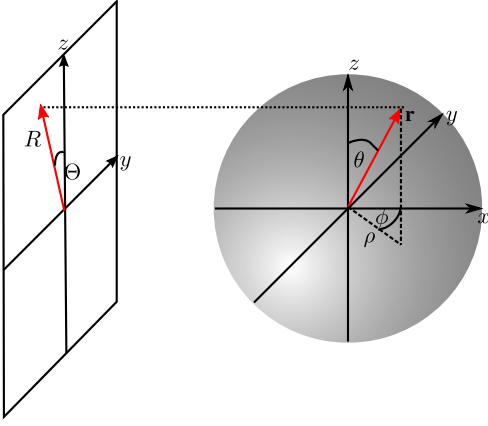
[a)]Electronic mail: j.underwood@ucl.ac.uk

FIG. 1. Relationship between coordinates of the original 3D Newton sphere (right) and the 2D projected image (left).

can subsequently be deconvoluted from the CEI images of aligned/oriented samples.

II. INVERSION OF PHOTOFRAGMENT IMAGES WITH NON-UNIFORM DETECTION

In a photofragment imaging experiment, the Newton sphere of charged particles of interest is projected onto a 2D position sensitive detector via electrostatic lenses which accelerate the charged particles towards the detector. If the initial distribution is cylindrically symmetric about an axis parallel to the detector frame, then the 3D distribution and its 2D projection are related via the Abel transform,

$$F(y,z) = 2 \int_y^\infty \frac{\rho f(\rho, z)}{\sqrt{\rho^2 - y^2}} \, \mathrm{d}\rho, \tag{1}$$

where $F(y,z)$ is the 2D projection, $f(\rho, z)$ is the 3D distribution which is assumed cylindrically about the z axis, and ρ is the distance to the z-axis as illustrated in Fig. 1. Typically, solving the inverse of this equation to recover the desired $f(\rho, z)$ distribution directly is sub-optimal due to the sensitivity to experimental noise, and consequently over the years a number of numerical approaches have been developed to tackle this problem.[1,7–9,30,31]

Here we treat the case where the 3D charged particle distribution lacks an axis of cylindrical symmetry due to a non-uniform detection function. We choose to analyse the problem in polar coordinates, which has been shown to have advantages in terms of localizing any noise in the inversion process to the very centre of the image,[9,30,31] and also provides a natural description of many optically induced processes in atoms and molecules.[32]

We consider the case where we wish to characterize a 3D cylindrically symmetric distribution $g(r,\theta)$, which is projected onto the detector via a non-uniform detection function $D(r,\theta,\phi)$. Here r, θ, and ϕ are respectively the radius, polar angle and azimuthal angle describing the position of a charged particle on the Newton sphere which is projected onto the detector (see Fig. 1). We show in Appendix A that the Abel transformation may be written in spherical polar coordinates as

$$\begin{aligned} F(R,\Theta) &= \int_R^\infty \frac{r f(r,\theta,\phi)}{\sqrt{r^2 - R^2}} \, \mathrm{d}r \\ &= \int_R^\infty \frac{r g(r,\theta) D(r,\theta,\phi)}{\sqrt{r^2 - R^2}} \, \mathrm{d}r. \end{aligned} \tag{2}$$

where $F(R,\Theta)$ is the projected (image) distribution, Θ is the polar angle measured in the detection plane with respect to the z axis, and R is the distance from the image centre (see Fig. 1).

Since Eq. (2) has a similar form to Eq. (1) many of the numerical approaches to inverting Eq. (1) could be adapted to invert Eq. (2) to obtain $g(r,\theta)$. Here we choose to adapt the widely used pBasex approach[9] and expand the desired distribution $g(r,\theta)$ as a product of basis functions comprising products of Gaussian radial functions and Legendre polynomials as angular functions,

$$g(r,\theta) = \sum_{k=0}^{k_{\max}} \sum_{l=0}^{l_{\max}} C_{kl} g_{kl}(r,\theta), \tag{3}$$

where the basis functions are

$$g_{kl}(r,\theta) = \frac{1}{\sigma\sqrt{2\pi}} \mathrm{e}^{-\frac{(r-r_k)^2}{2\sigma^2}} P_l(\cos\theta). \tag{4}$$

Each radial function has a Gaussian width of σ and is centred at $r_k = \Delta r_k k$ where $\Delta r_k = r_{\max}/k_{\max}$ and $r_{\max}$ is the maximum radius of the charged particle cloud considered.

The VMI image $F(R,\Theta)$ can then be written as an expansion in the corresponding projected basis functions,

$$F(R,\Theta) = \sum_{k=0}^{k_{\max}} \sum_{l=0}^{l_{\max}} C_{kl} F_{kl}(R,\Theta), \tag{5}$$

where the projected basis functions are given by

$$F_{kl}(R,\Theta) = \int_R^\infty \frac{r g_{kl}(r,\theta) D(r,\theta,\phi)}{\sqrt{r^2 - R^2}} \, \mathrm{d}r. \tag{6}$$

In the common case where the projected image is detected on a discrete grid of cartesian pixels, so long as we choose the width σ of the radial basis functions in Eq. (3) to be around 1 pixel, we can express the image Eq. (5) in discrete form as

$$F_{ij}(R_i,\Theta_j) = \sum_{k=0}^{k_{\max}} \sum_{l=0}^{l_{\max}} C_{kl} F_{kl}^{ij}(R_i,\Theta_j), \tag{7}$$

where i and j are the detector radial and angular pixel indices respectively. Here $R_i = (i + \frac{1}{2})\Delta R$ is the value of R at the centre of pixel (i,j), where ΔR is the radial pixel width, and $\Theta_j = (j + \frac{1}{2})\Delta\Theta$ is the value of Θ at the

centre of the pixel (i, j), where $\Delta\Theta$ is the angular pixel width. The corresponding discretized basis functions are given by

$$F_{kl}^{ij}(R_i, \Theta_j) = \int_{R_i}^{\infty} \frac{r g_{kl}(r, \theta) D(r, \theta, \phi)}{\sqrt{r^2 - R_i^2}} \, \mathrm{d}r, \qquad (8)$$

where

$$\cos\theta = \frac{R_i \cos\Theta_j}{r} \qquad (9)$$

$$\sin\phi = \frac{R_i \sin\Theta_j}{r \sin\theta} = \frac{R_i \sin\Theta_j}{\sqrt{r^2 - R_i^2 \cos^2\Theta_j}} \qquad (10)$$

The basis functions Eq. (8) represent the VMI images corresponding to each basis function $g_{kl}(r, \theta)$ convoluted with the detection function $D(r, \theta, \phi)$. These projected basis functions may be calculated using standard numerical integration methods such as CQUAD in the GSL library[33] to perform the integration over r in Eq. (8). In order to obtain the expansion coefficients C_{kl}, the system of linear equations represented by the matrix equation Eq. (7) can then be solved using linear algebra techniques such as singular value decomposition.[9,33] We note that the method as described is identical to pBasex[9] in the limit $D(r, \theta, \phi) = 1$.

Once fitted, the C_{kl} coefficients can be used to characterize the charged particle distribution by calculating the angular integrated radial spectrum (which is related to the speed distribution of the particles) according to

$$I(r) = \frac{1}{\sigma\sqrt{2\pi}} \sum_{k=0}^{k_{\max}} C_{k0} \mathrm{e}^{-\frac{(r-r_k)^2}{2\sigma^2}}. \qquad (11)$$

In addition, it is usual to characterize the (radially dependent) angular distribution according to an expansion in Legendre polynomials $P_l(\cos\theta)$,

$$f(\theta; r) = \frac{1}{\sqrt{4\pi}} \sum_{l=0}^{l_{\max}} \beta_l(r) P_l(\cos\theta), \qquad (12)$$

where the β_l coefficients are calculated from the C_{kl} coefficients as

$$\beta_l(r) = \frac{\sum_{k=0}^{k_{\max}} C_{kl} \mathrm{e}^{-\frac{(r-r_k)^2}{2\sigma^2}}}{\sum_{k=0}^{k_{\max}} C_{k0} \mathrm{e}^{-\frac{(r-r_k)^2}{2\sigma^2}}}, \qquad (13)$$

which are normalized to $\beta_0(r) = 1$.

III. APPLICATION TO MOLECULAR AXIS ALIGNMENT AND ORIENTATION PROBED BY COULOMB EXPLOSION IMAGING

A. Methodology

We turn now to the application of the formalism presented in Sec. II to the measurement of molecular axis alignment and orientation from Coulomb explosion imaging with VMI detection.[13–15,17–19]

As described in the introduction, in such experiments, the molecular sample is first aligned/oriented with strong non-resonant laser fields (and sometimes static electric fields). Subsequently, in order to measure the degree of alignment/orientation produced, an intense probe laser pulse with duration much shorter than molecular rotation is used to remove multiple electrons from the molecules under study. The multiply ionized molecules subsequently undergo rapid fragmentation due to Coulomb repulsion, and imaging of the resulting ion fragments is then used to establish the molecular axis distribution prior to ionization. Under the assumptions that the fragmentation happens rapidly with respect to rotation, and that the fragments recoil in the direction of molecular bonds, there is a direct correlation between the fragment recoil and the molecular orientation. As mentioned previously, the challenge here is to deconvolute the non-uniform orientational response of the Coulomb explosion process from the measurement in order to yield the molecular axis distribution prior to Coulomb explosion. The strategy we propose here is:

1. Perform a CEI measurement on an isotropic gas sample, with the CEI probe polarization direction chosen such that an axis of cylindrical symmetry is contained in the plane of the detector.

2. Invert the image from step 1 above to obtain the 3D distribution of CEI ions by solving Eq. (7) with $D(r, \theta, \phi) = 1$. Since this distribution was obtained with an isotropic gas sample, we can obtain the orientational dependence of the CEI probe process for the CEI probe laser polarization state, pulse duration and intensity employed in step 1 above.

3. Perform a CEI measurement on the aligned/oriented molecular sample using the same probe polarization state, pulse duration and intensity as used in step 1 above.

4. Invert the VMI image from step 3 using Eq. (7) and a detection function derived from step (2) in order to deconvolute the orientational dependence of the CE process from the observed fragment distribution, and so obtain the molecular axis distribution.

We note that we require the molecular axis distribution in step 3 above to have an axis of cylindrical symmetry lying in the plane of the detector in order to apply Eq. (7). However, step 3 does <u>not</u> require that the same geometry of the probe is used as for step 2. For example, if using a linearly polarized probe, step 2 requires that the linear polarization lies in the plane of the detector, but in step 3 we are free to rotate the probe polarization to lie in a different direction such as perpendicular to the detector plane. For this reason we introduce two frames of reference: (i) the detection frame (DF); and (ii) the

axis distribution frame (AF). In order to invert the observed image in step 2, we require that the DF possesses an axis of cylindrical symmetry lying in the plane of the detector in step 1. As such, the detection function will have an axis of cylindrical symmetry in the DF. We also require that the molecular axis distribution possesses an axis of cylindrical symmetry in the plane of the detector in step 3. However, in step 3, the DF may be chosen to lie in any direction relative to the AF.

The inversion of the image recorded for the isotropic molecular sample in step 2 will yield the fit coefficients for the distribution of fragments, C'_{kl}. Here, and in what follows, we use a prime to denote properties relating to the detection function. Under the assumption that the fragments recoil along the direction of the molecular bond, this distribution will correspond to the probability of CE for each orientation of that bond relative to the laser polarization, and so these coefficients can be used to construct the orientational detection function required for step 4.

In the reference frame defined by the detection laser polarization, we can write the orientational dependence of the CE probe as

$$D(\theta'; r) = \frac{1}{\sqrt{4\pi}} \sum_l^{l_{\max}} \beta'_l(r) P_l(\cos\theta'), \qquad (14)$$

where θ' is measured relative to the cylindrical symmetry axis in the DF. The expansion coefficients $\beta'_l(r)$ are calculated from the fit coefficients C'_{kl} according to Eq. (13).

In order to construct the basis functions Eq. (8) for step 4, we need to calculate the detection function in the AF. The angular dependence of the detection function expressed in the DF, $D(\theta', \phi'; r)$ is related to the angular dependence of the detection function in the AF, $D(\theta, \phi; r)$ through a rotation through the Euler angles (α, Ω, γ) connecting the AF and DF.[34] For the present case where the detection function has an axis of cylindrical symmetry, we can set $\gamma = 0°$. In Appendix B we show that the detection function in the AF may be expressed in terms of the $\beta'_l(r)$ coefficients found from the probe-alone data inversion as

$$D(\theta, \phi; r) = \frac{1}{\sqrt{4\pi}} \sum_l \beta'(r) P_l(\cos\Delta), \qquad (15)$$

where

$$\cos\Delta = \cos\Omega\cos\theta + \sin\Omega\sin\theta\cos(\alpha - \phi)$$
$$= \cos\Omega\cos\theta + \sin\Omega\sin\theta(\cos\alpha\cos\phi + \sin\alpha\sin\phi). \qquad (16)$$

Eqs. (15) and (16) allow for the evaluation of $D(r, \theta, \phi)$ in Eq. (8) during the numerical integration over r when calculating the basis functions.

It is important to note that steps 1 and 2 allow us to retrieve $D(\theta, \phi; r)$, a detection function dependent upon two of the Euler angles (θ, ϕ) describing molecular orientation in the AF. As such, this detection function is averaged over the third Euler angle χ that would be needed to specify the molecular orientation.[34] This angle describes rotation of the molecule around the molecular z-axis. As such, this strategy is applicable to extracting the alignment/orientation of linear molecules and symmetric rotor molecules. For asymmetric rotor molecules where localization in χ accompanies localization in θ[13,17,35] care must be taken, and this approach will only apply when either the localization in χ is small and/or $D(\theta, \phi, \chi; r)$ is independent of χ. The latter situation arises for many molecules.

B. Experimental example

As a demonstration of the approach outlined in Subsection III A, we apply the strategy to the retrieval of the molecular axis distribution of a sample of 1,4-diiodobenzene (pDIB) molecules aligned with a strong laser field at 1064 nm wavelength.[36] For this molecular species, a strong linearly polarized laser field will induce alignment of the I-I axis (the most polarizable axis) towards the laser field polarization direction. CEI was used to characterize the alignment of the I-I axis, through detection of recoiling I^+ fragments. Under the assumption that the I^+ fragments recoil axially along the C-I bonds in the molecule, the I^+ recoil direction maps directly to the I-I axis direction in the lab frame. For this molecule, we expect the dependence of the detection function on the angle χ to be negligible.

The molecular sample was prepared in a molecular beam with a rotational temperature of ca. 1-2 K. The linearly polarized alignment laser field had a pulse duration of 10 ns which is much longer than the time scale for molecular rotation. Consequently, this laser field adiabatically induces molecular axis alignment of the I-I axis in the sample, with maximal alignment occurring at the peak of the laser field.[16,37] Subsequently a second probe laser pulse at 800 nm and with duration of 30 fs was timed to arrive at the peak of the alignment laser field. This high intensity laser pulse induced Coulomb explosion of the aligned molecules, and the I^+ ions produced were detected with a VMI spectrometer.

We report here the results of two different studies. In the first study a circularly polarized probe laser pulse was employed, and the alignment using two different intensities of the aligning laser pulse are compared. In the second study a linearly polarized probe laser pulse was employed, and we examine the effect of the probe geometry employed by comparing images recorded with the probe polarization either parallel or perpendicular to the aligning laser polarization.

1. Circularly polarized probe pulse

Here we detail experiments carried out with a circularly polarized laser pulses with intensity of 2×10^{14} W/cm². In Fig. 2a we show the I^+ VMI data
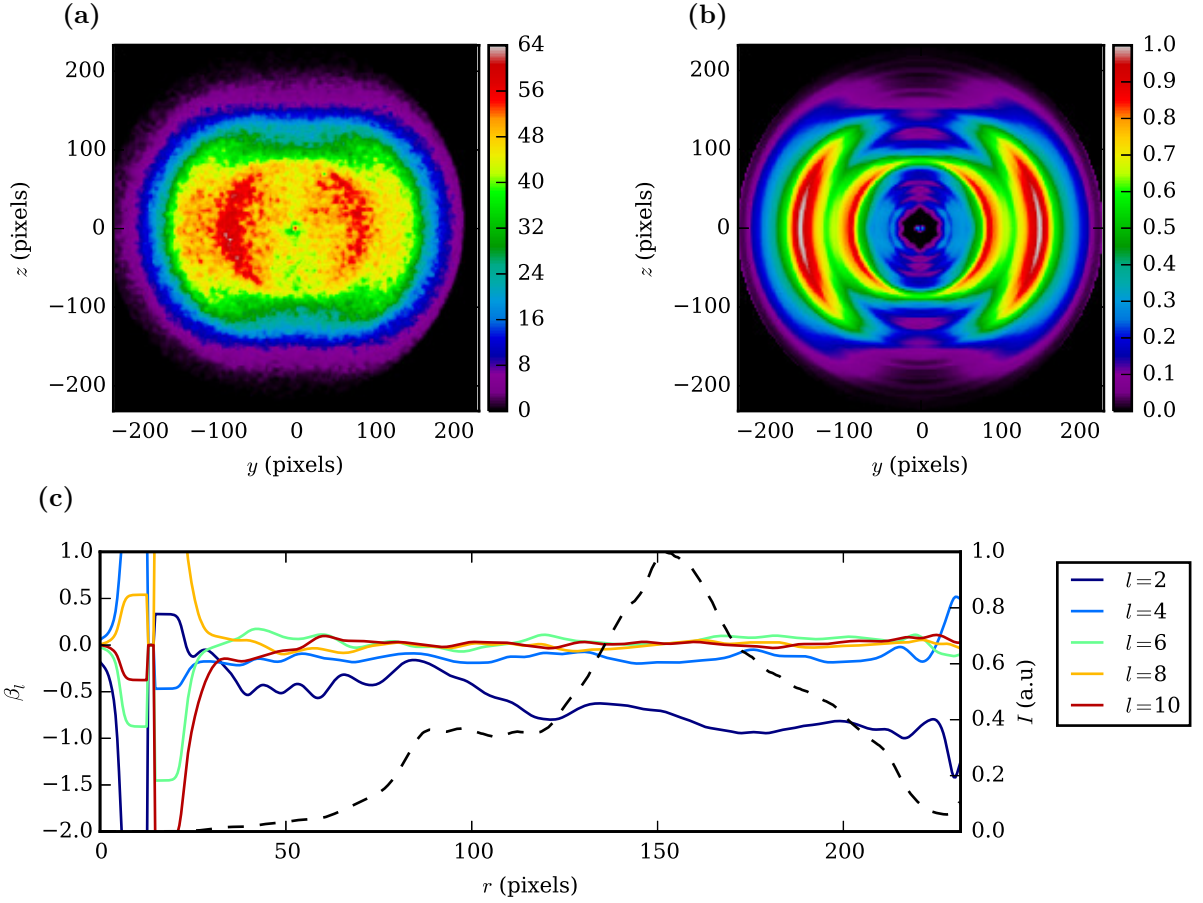
(a)

(b)

(c)

FIG. 2. (a) Experimental I$^+$ VMI image recorded for the circularly polarized probe laser alone. The axis of cylindrical symmetry (corresponding to the laser propagation direction) lies parallel to the z-axis. (b) Corresponding pBasex inverted I$^+$ image. (c) Radial dependence of the $\beta_l(r)$ angular parameters corresponding to the pBasex inverted image (solid lines). The radial spectrum is also shown (dashed line).

recorded for the circularly polarized probe alone. Two radially separated rings are seen corresponding to two different CE channels. The outermost channel corresponds to CE of triply charged pDIB molecules whereas the innermost ring results from CE of doubly charged pDIB molecules.[38] Fig. 2b shows the distribution of I$^+$ ions obtained from the pBasex inversion of the experimental VMI image. This inversion was carried out by binning the experimental image into a 256×256 polar image and solving Eq. (7) with $k_{\max} = 128$, $l_{\max} = 10$, $D(r, \theta, \phi) = 1$ (i.e. uniform detection), and $\sigma = 1.2$ pixels. The coefficients C_{kl} in Eq. (7) were obtained through projected Landweber iteration[39,40] with a projection function setting $C_{kl} = 0$ if $C_{k0} < 0$ at each iteration. Further, due to the inversion symmetry of the experiment, only even values of l were included in Eq. (7).

In Fig. 2c we show the $\beta_l(r)$ parameters calculated according to Eq. (13), as well as the radial spectrum calculated from Eq. (11). From this plot we can see that in regions with non-negligible ion intensity, contributions from $\beta_l(r)$ parameters with $l > 4$ are negligible, and as such the probe detection function is well defined by C_{kl}

coefficients with $l \leq 4$.

The distribution shown in Fig. 2b represents the detection function for CEI probing with the circularly polarized laser pulse for the intensity and pulse duration used. It is this distribution that samples the aligned axis distribution in the subsequent measurements with laser-aligned molecular samples.

In Fig. 3(a) and Fig. 3(b) we show the I$^+$ VMI data recorded for a sample of molecules aligned with linearly polarized laser fields of intensities 1.5×10^{11} W/cm^2 and 7.7×10^{11} W/cm^2 respectively. The aligning laser field was polarized parallel to the z-axis. This laser field therefore induces alignment of the molecular I-I-axis towards the z-axis. The circularly polarized CE pulse propagated parallel to the y-axis such that the light was polarized in the xz-plane. The observed VMI image therefore corresponds to the molecular axis distribution sampled by the detection function of the probe.

In Fig. 3c and Fig. 3d we show the recovered distributions of I$^+$ ions following deconvolution of the detection function determined from the probe alone data following the procedure outlined in Subsection III A. The in-
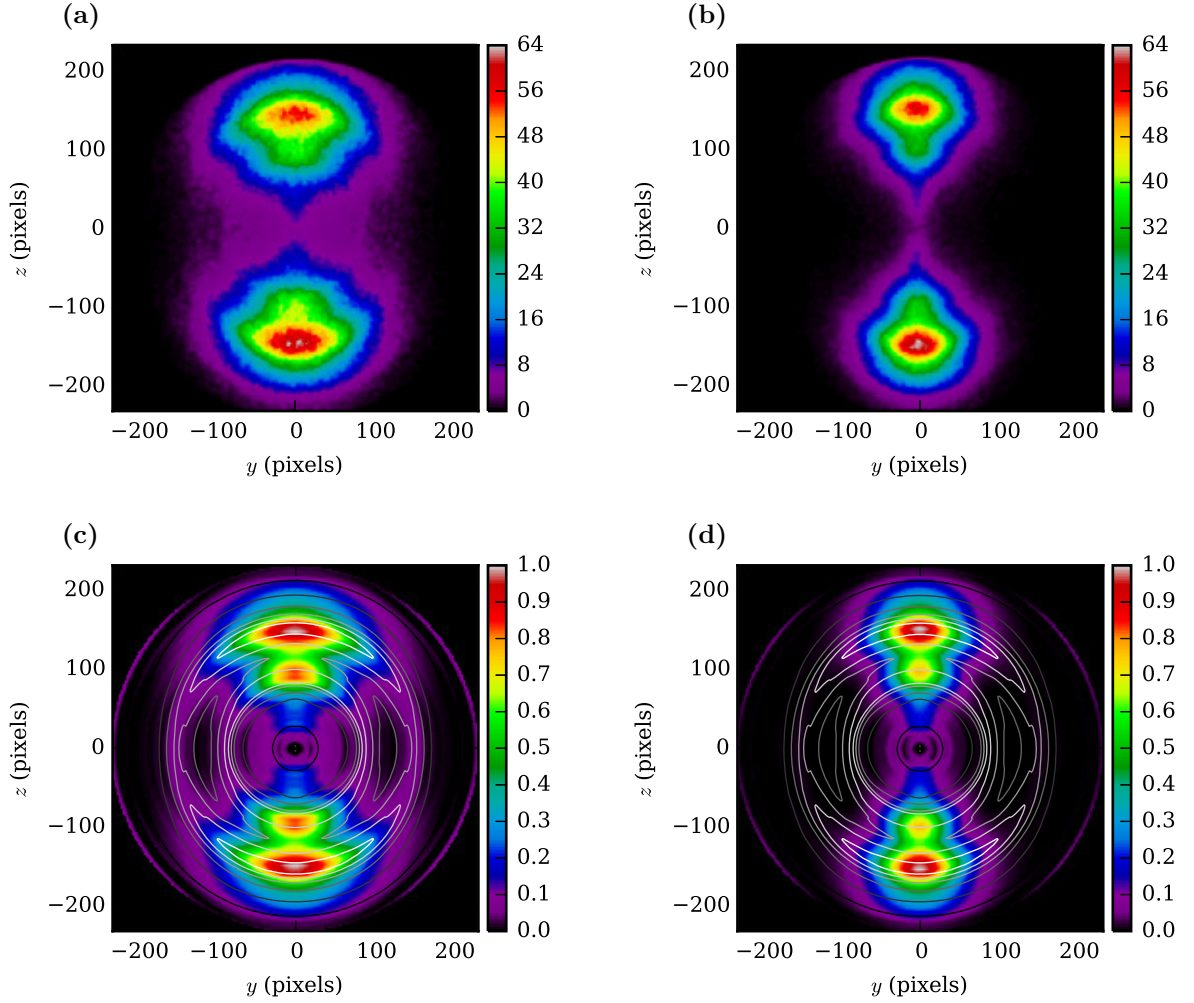
(a)

(b)

(c)

(d)

FIG. 3. (a) and (b): Experimental I^+ VMI images recorded for laser aligned pDIB probed via Coulomb explosion with a circularly polarized laser pulse. The aligning laser polarization is along z, and the probe propagation direction lies along y. Images are shown for aligning laser field intensities of (a) 1.5×10^{11} W/cm^2, and (b) 7.7×10^{11} W/cm^2. (c) and (d): Corresponding pBasex inverted I^+ images with detection function deconvoluted. Overlaid is a grayscale contour map corresponding to the probe alone distribution shown in Fig. 2b.

versions to recover these distributions were carried out with $l_{\max} = 14$ and $k_{\max}$, σ and the number of polar bins the same as for the probe-alone data. The detection function $D(r, \theta, \phi)$ used to construct the basis functions (Eq. (8)) was calculated from Eq. (14) with Δ calculated from Eq. (16) setting $\Omega = 90°$ and $\alpha = 0°$. The coefficients C_{kl} in Eq. (7) were obtained through Landweber iteration with no projection function.[39,40] Further, due to the inversion symmetry of the experiment, only even values of l were included in Eq. (7).

Overlaid on each recovered distribution in Fig. 3c and Fig. 3d is a grayscale contour map corresponding to the probe detection function axially integrated over the azimuthal angle ϕ. The calculation of this axially integrated detection function is detailed in Appendix C. This contour map provides a visual representation of the detection function – its value represents the detection probability at each value of θ integrated over all values of ϕ.

As can be seen from inspection of Fig. 3c and Fig. 3d, the probe detection function samples the molecular axis distribution with high efficiency for both aligning laser intensities.

The degree of overlap of the detection function with the axis distribution determines the extent to which the full molecular axis distribution is sampled, and the reliability of the deconvolution process. We can quantify the degree of this overlap by evaluating the angular overlap factor

$$O(r) = \frac{1}{D_{\max}(r)} \int_0^{2\pi} \mathrm{d}\phi \int_0^{\pi} \sin\theta \, \mathrm{d}\theta f(\theta; r) D(\theta, \phi; r),$$
(17)

where $D_{\max}(r)$ is the maximum value of the angular dependence of the detection function in the AF, $D(\theta, \phi; r)$. This integral will take values between 0 (no overlap) and 1 (maximal overlap). The evaluation of this integral is detailed in Appendix D. In Fig. 4 we show the radial depen-
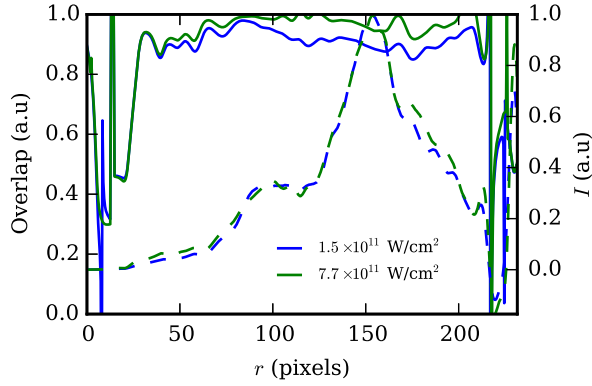
FIG. 4. Radial dependence of the angular overlap factor corresponding to the pBasex inversion of the images shown in Fig. 3 (solid lines) for alignment laser intensities of 1.5×10^{11} W/cm^2 and 7.7×10^{11} W/cm^2, and a circularly polarized probe. The corresponding radial spectra are also shown (dashed lines).

dence of the this overlap factor for the two aligning laser intensities employed. The overlap factor is clearly lower for the less well aligned distribution at the lower aligning laser intensity, reflecting the fact that the broader axis distribution extends further into the region of lower probability of CE by the probe laser pulse, as is also seen by comparing Fig. 3c and Fig. 3d. Nonetheless in both cases the overlap factor is above 0.9 signifying good sampling of the axis distribution.

In Fig. 5 we show the $\beta_l(r)$ parameters calculated according to Eq. (13), as well as the radial spectrum calculated from Eq. (11). For both intensities employed, the resulting $\beta_{14}(r)$ coefficient remained at 0, and increasing the value of $l_{\max}$ beyond 14 led to no significant change in the inverted image. These observations indicate that the alignment distribution is well characterized with $l_{\max} = 14$. At the lower intensity of 1.5×10^{11} W/cm^2 all β_l coefficients are seen to be smaller in magnitude than for the higher intensity of 7.7×10^{11} W/cm^2, and indeed at the lower alignment laser intensity the $\beta_{10}(r)$ coefficient was seen to be negligible. This is consistent with the high alignment laser intensity producing a higher degree of molecular axis alignment. In both cases, some large fluctuation in $\beta_l(r)$ values is observed at the largest values of r due to the experimental image being slightly truncated by the detector edge.

In Fig. 6 we show the $\langle \cos^2 \theta \rangle(r)$ expectation values for the data as well as the radial spectrum calculated from Eq. (11). This expectation value is a commonly used figure-of-merit for characterizing the degree of molecular axis alignment. It is important to note that this is an expectation value of the molecular axis distribution, rather than the commonly used value $\langle \cos^2 \Theta \rangle$, referred to as $\langle \cos^2 \theta_{2D} \rangle$, which is an expectation value of the projected image of the axis distribution and which includes the effect of the non-uniform detection function. The

value of $\langle \cos^2 \theta \rangle(r)$ was calculated acording to

$$\langle \cos^2 \theta \rangle(r) = \int_0^\pi \sum_{l=0}^{l_{\max}} \beta_l(r) P_l(\cos \theta) \cos^2 \theta \sin \theta \, d\theta. \quad (18)$$

We note that for both aligning laser intensities, the outermost channel ($r \sim 150$ pixels) indicates a slightly higher degree of molecular axis alignment than the innermost channel ($r \sim 100$ pixels) – this is evidenced by the smaller values of the β_l parameters for the inner channel compared to the outer channel in Fig. 5, and to a lesser extent by the $\langle \cos^2 \theta \rangle$ expectation values for each channel. As mentioned, the I$^+$ signal in the outermost channel mainly originates from Coulomb explosion of triply charged molecules whereas I$^+$ ions in the innermost channel mainly originate from doubly ionized molecules. The triply ionized molecules are produced in the region of the probe laser focus where the intensity is highest and therefore also in the region where the alignment laser intensity is highest. As such the outermost channel probes molecules that are expected to be slightly better aligned than molecules probed by the innermost channel. Additionally, in the preceding development of our methodology we have implicitly assumed that the fragment I$^+$ ions recoil axially along the direction of the molecular I-I axis such that there is a direct correspondence between fragment recoil and molecular axis alignment. It is possible that this axial recoil condition of the I$^+$ fragments is better fulfilled for the outermost channel than for the innermost channel. In general, some deviation from axial recoil is expected due to bonding in the multiply charged molecular ion created by the probe pulse and to possible charge-asymmetry in the Coulomb explosion process. The effect of the non-axial recoil is expected to slightly reduce the degree of measured alignment and it is not removed by our deconvolution of the detection function – this will be discussed further in a future publication[38].

2. Linearly polarized probe pulse

Here we detail a second study carried out with a linearly polarized probe pulse of intensity 3.2×10^{14} W/cm^2, and a linearly polarized aligning pulse of intensity 6.6×10^{11} W/cm^2. In Fig. 7a we show the VMI data recorded for the probe laser alone with its polarization along the z-axis. The same two CEI channels as observed with the circularly polarized probe pulse are evident in the VMI data. Fig. 7b shows the corresponding distribution of I$^+$ ions obtained from the pBasex inversion of the VMI image. The lower number of counts in this image (due to a reduced data collection time) required a more coarse binning of the data when carrying out the pBasex inversion compared to the circularly polarized probe case. The experimental image was binned into a 128×128 polar image and Eq. (7) was solved with $k_{\max} = 64$, $l_{\max} = 10$, $D(r, \theta, \phi) = 1$ (i.e. uniform detection), and
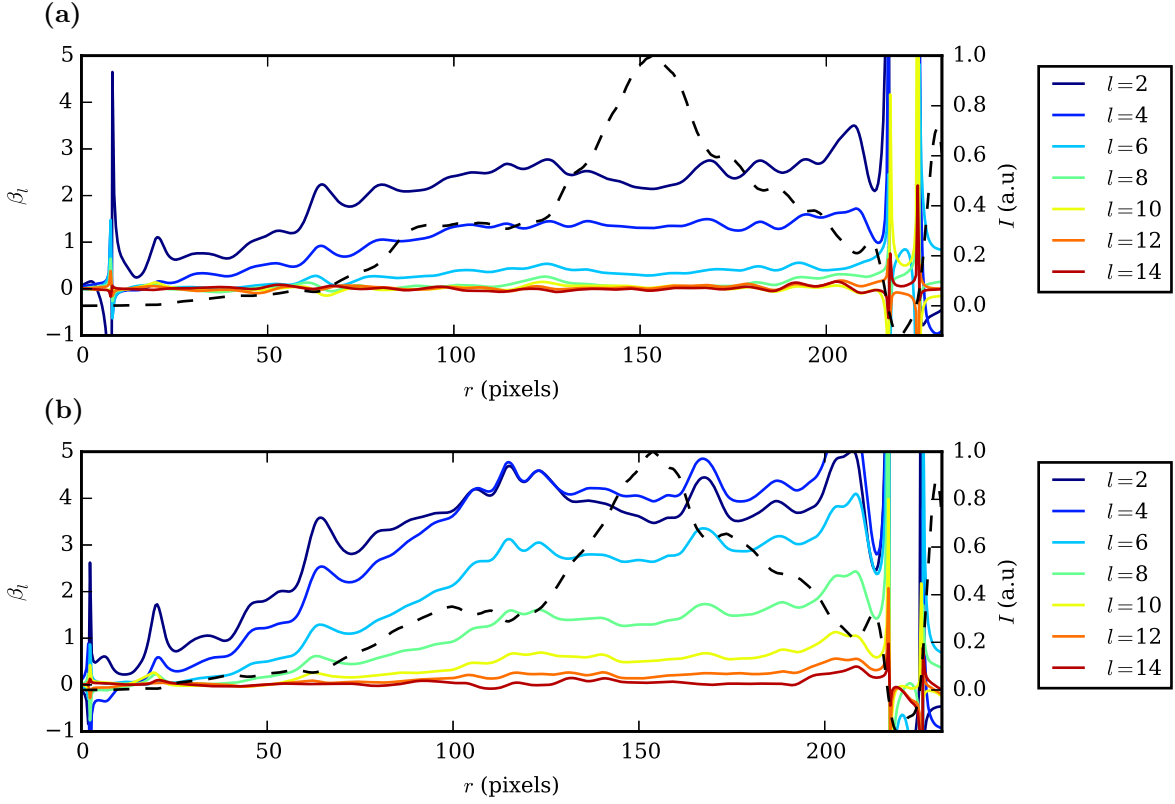
(a)

(b)

FIG. 5. Radial dependence of the $\beta_l(r)$ angular parameters obtained from the deconvoluted pBasex inversion of the images shown in Fig. 3 (solid lines). (a) alignment laser intensity of 1.5×10^{11} W/cm^2. (b) alignment laser intensity of 7.7×10^{11} W/cm^2. The corresponding radial spectra are also shown (dashed lines).
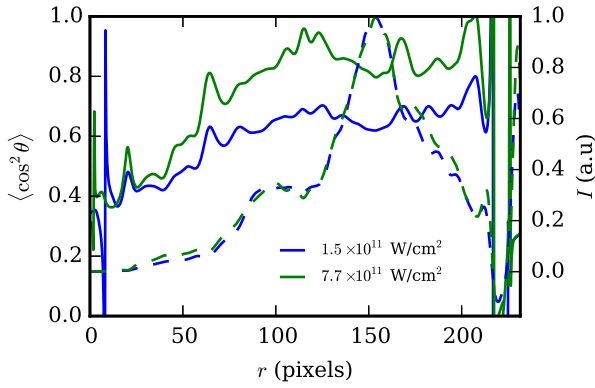

FIG. 6. Radial dependence of the $\langle \cos^2 \theta \rangle$ expecatation values resulting from inversion of the images shown in Fig. 3 (solid lines) for the two alignment laser intensities of 1.5×10^{11} W/cm^2 and 7.7×10^{11} W/cm^2, and a circularly polarized probe laser. The corresponding radial spectra are also shown (dashed lines).

$\sigma = 1.75$ pixels. The coefficients C_{kl} in Eq. (7) were obtained through projected Landweber iteration[39,40] with a projection function setting $C_{kl} = 0$ if $C_{k0} < 0$ at each iteration. As previously, only even values of l were included in Eq. (7).

In Fig. 7c we show the $\beta_l(r)$ parameters calculated according to Eq. (13), as well as the radial spectrum calculated from Eq. (11). As was the case with the circularly polarized probe pulse, in regions with non-negligible ion intensity, contributions from $\beta_l(r)$ parameters with $l > 4$ are negligible.

In Fig. 8a and Fig. 8b we show VMI data recorded for molecules aligned with a linearly polarized laser field and probed with a linearly polarized probe pulse in two different geometries. For the data in Fig. 8a a parallel geometry was employed with both the aligning and probe laser polarizations along the z-axis. In Fig. 8b a perpendicular geometry was used with the aligning laser field polarized along the z-axis and the probe laser field polarized along the x-axis (perpendicular to the detection plane). From these images it is apparent that the relative magnitude of the two CEI channels depends strongly on the orientation of the probe pulse polarization relative to the molecular axis.

In Fig. 8c and Fig. 8d we show the distributions of I$^+$ ions following deconvolution of the detection function determined from the probe alone data following the procedure outlined in Sec. III A. Overlaid on each recovered distribution in Fig. 8c and Fig. 8d is a grayscale contour map corresponding to the probe detection function axially integrated over the azimuthal angle ϕ (Appendix
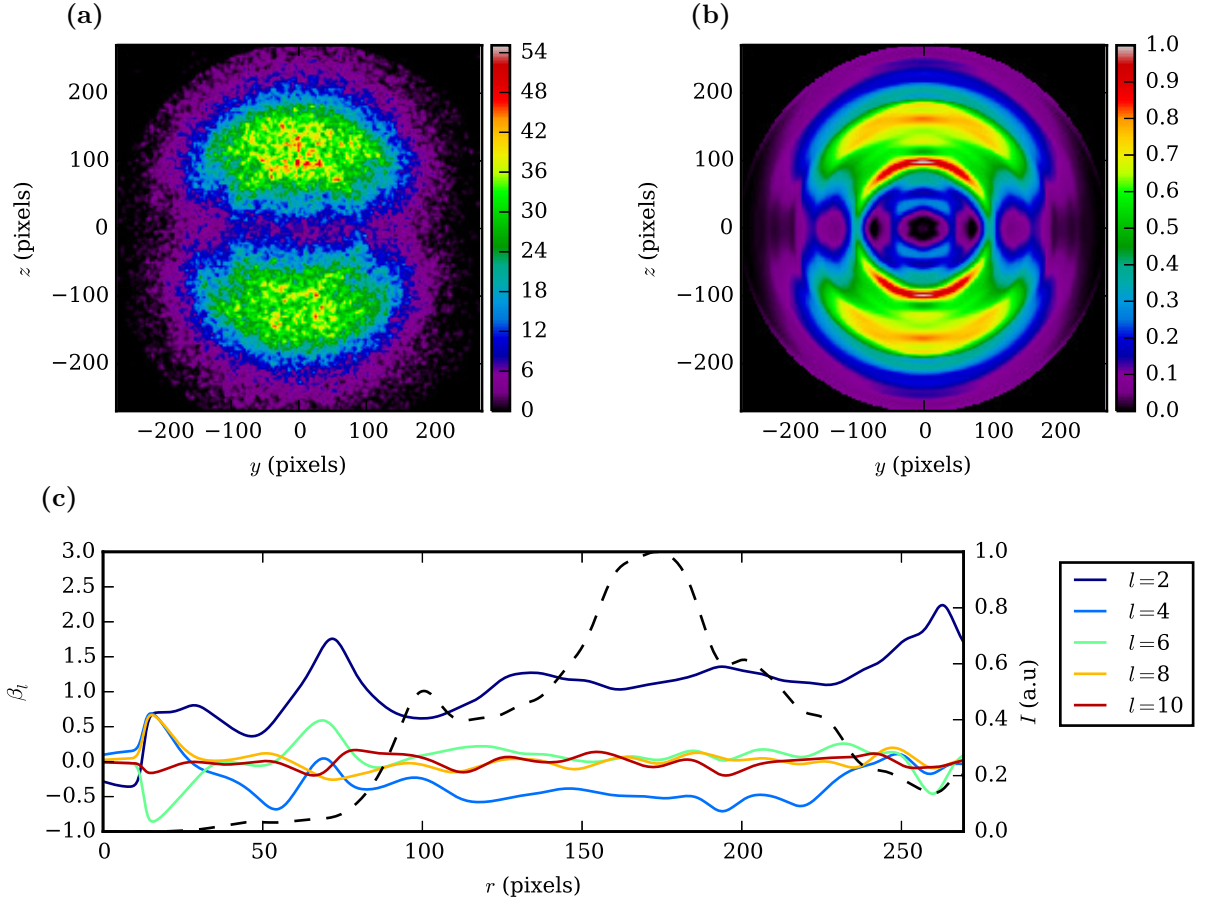
(a)

(b)

(c)

FIG. 7. (a) Experimental I$^+$ VMI image recorded for the linearly polarized probe laser alone. The axis of cylindrical symmetry (corresponding to the laser propagation direction) lies parallel to the z-axis. (b) Corresponding pBasex inverted I$^+$ image. (c) Radial dependence of the $\beta_l(r)$ angular parameters corresponding to the pBasex inverted image (solid lines). The radial spectrum is also shown (dashed line).

C). As can be seen from comparing Fig. 8c and Fig. 8d, the probe detection function samples the axis distribution with much lower efficiency when the probe polarization is along the x-axis, perpendicular to the direction of molecular alignment. Note that in Fig. 8d, the axially integrated detection function has a higher efficiency along the y-axis than the z-axis due to the integration over ϕ encompassing the x-axis for $\theta = 90°$.

The inversions to recover the distributions in Fig. 8 were carried out by binning the experimental image into a 256×256 polar image and solving Eq. (7) with $k_{\max} = 128$, $l_{\max} = 20$, and $\sigma = 1.2$ pixels. The detection function $D(r,\theta,\phi)$ used to construct the basis functions (Eq. (8)) was calculated from Eq. (14) with Δ calculated from Eq. (16) setting $\Omega = 0°$ and $\alpha = 0°$ for the parallel geometry and $\Omega = 90°$ and $\alpha = 0°$ for the perpendicular geometry. The coefficients C_{kl} in Eq. (7) were obtained through singular value deconvolution[33] which was found to give satisfactory results without requiring regularization via the projected Landweber iteration. As previously, only even values of l were included in Eq. (7).

The radial spectra obtained from the deconvolution

calculated according to Eq. (11) shown in Fig. 9 clearly show that for the perpendicular probe geometry there is a reduced relative contribution from the outer CEI channel, corresponding to explosion of the triply charged parent ion, compared to the doubly charged parent ion CEI channel. In addition, other features are observed in the perpendicular geometry radial spectra suggesting that the relative contributions from different fragmentation pathways are dependent on molecular orientation.[41] It is interesting to note that these details would not be apparent from the raw VMI data before deconvolution/inversion.

In Fig. 10 we show the radial dependence of the angular overlap integral (Eq. (17) evaluated as described in Appendix D). This plot shows that the perpendicular probing geometry has a much lower angular overlap integral than the parallel probe geometry, and also the circularly polarized probe described in Subsection III B 1(see Fig. 4). This is due to the fact that for this molecule the ionization probability for these CEI channels is greatest when the probe laser polarization lies along the I-I molecular axis. However, the ionization probability does not
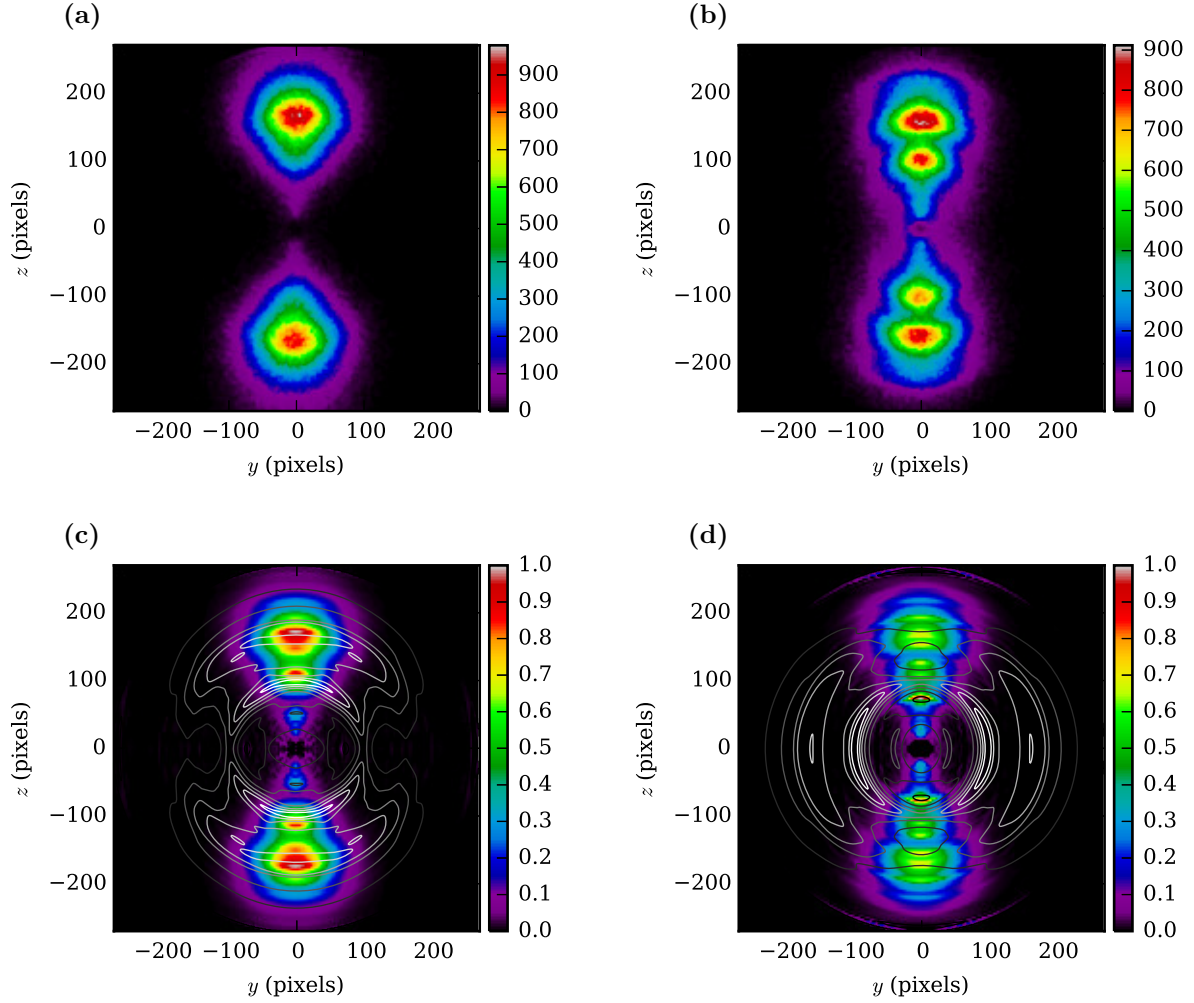
FIG. 8. (a) and (b): Experimental I^+ VMI images recorded for laser aligned pDIB probed via Coulomb explosion with a linearly polarized probe laser pulse. The aligning laser pulse was polarized along the z direction. In (a) the probe laser was also polarized along the z-axis. In (b) the probe laser was polarized along the x-axis (perpendicular to the detector plane). (c) and (d): Corresponding pBasex inverted I^+ images with detection function deconvoluted. Overlaid is a grayscale contour map corresponding to the ϕ-integrated detection function.

drop to zero when the probe laser is perpendicular to the I-I axis. One advantage of the perpendicular probe geometry is that, for molecules with their I-I axes lying in the yz-plane, there is uniform ionization probability with respect to molecular rotation about the x axis – as such this provides a good measurement of the degree of localization of the I-I molecular axes towards the z-axis for those in-plane molecules. It is interesting to note that for the perpendicular probe geometry, the inner (doubly charged parent) channel has a higher overlap integral than the outer (triply charged parent) channel, showing that the inner channel's dependence on molecular orientation is weaker than that for the outer channel.

Fig. 11 shows the radial dependence of the $\langle \cos^2 \theta \rangle$ expectation value for the parallel and perpendicular probe geometries calculated according to Eq. (18). For the outer channel the retrieved $\langle \cos^2 \theta \rangle$ is ca. 0.90 for both the parallel and the perpendicular probe geometry. It

might have been expected that the higher angular overlap factor for the parallel probe geometry would lead to a higher retrieved value of $\langle \cos^2 \theta \rangle$ value compared to that for the perpendicular probe geometry. On the other hand in the parallel geometry the best aligned molecules have their I-I axis close to the polarization axis of the probe pulse and as such they have an increased probability of being ionized to higher charge states due to enhanced ionization.[42–47] These higher charged molecular ions could fragment into I^{n+} ions with $n > 1$ rather than into I^+, i.e. the best aligned molecules would not lead to signal in the I^+ ion images and would therefore lead to a reduced value of $\langle \cos^2 \theta \rangle$ when determined from the I^+ signal. The almost identical $\langle \cos^2 \theta \rangle$ value observed for the parallel and perpendicular geometries indicates that neither the detection overlap factor nor enhanced ionization prevents a reliable measurement of the degree of alignment for any of the probe geometries using the
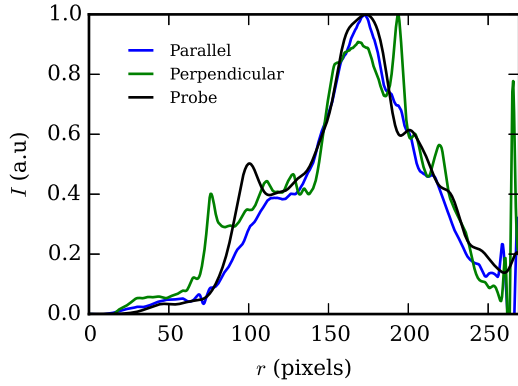
FIG. 9. Radial spectra obtained from the pBasex inversion of the aligned molecule data (Fig. 8) for the parallel (blue) and perpendicular (green) probing geometries. The radial spectrum obtained from pBasex inversion of the probe-alone data for randomly oriented molecules (Fig. 7) is also shown (black). All spectra shown are normalized to a maximum value of 1.
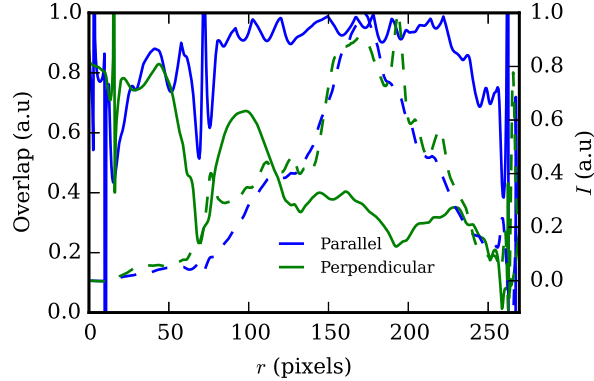

FIG. 10. Radial dependence of the angular overlap factor corresponding to the pBasex inversion of the images shown in Fig. 8 (solid lines) for the parallel and perpendicular probing geometries. The corresponding radial spectra are also shown (dashed lines).

algorithm presented here. In addition, it is clear that although the relative weightings of different fragmentation channels depends on the molecular orientation (as seen from the radial spectra, Fig. 9),[41] this is correctly accounted for in the retrival algorithm presented, as evidenced by the consistent $\langle\cos^2\theta\rangle$ values for the two probe geometries. For the inner channel, the retrieved $\langle\cos^2\theta\rangle$ value is lower for the perpendicular probe geometry compared to the parallel probe geometry. Since both probe geometries are sampling an identical molecular axis distribution, the retrieved $\langle\cos^2\theta\rangle$ value should be the same in both cases, as is observed for the outer channel. As with the slightly reduced degree of alignment observed for the inner channel when probing with the circularly polarized probe in Subsection III B 1, we attribute this difference as arising due to non-axial recoil geometries
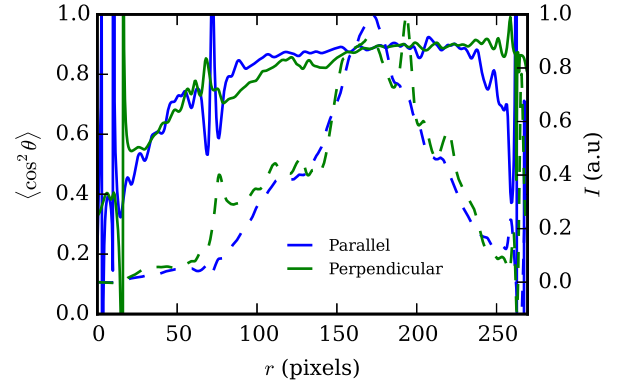

FIG. 11. Radial dependence of the $\langle\cos^2\theta\rangle$ expectation values obtained from the pBasex inversion of the data shown in Fig. 8 for the parallel (blue) and perpendicular (green) probe geometries. The radial spectra are also shown (dashed lines).

being active for the inner channel.[38]

In Fig. 12 we show the $\beta_l(r)$ parameters for both the parallel and perpendicular probe geometries calculated according to Eq. (13). In both cases these coefficients show there is negligible contribution from Legendre polynomials beyond 12 for the alignment laser intensity used. The $\beta_l(r)$ coefficients for the two probe geometries agree well for the outer CEI channel, but there is a decrease in the $\beta_l(r)$ coefficients for the perpendicular geometry similar to that seen with the $\langle\cos^2\theta\rangle$ expectation value.

IV. CONCLUSION

We have proposed a method for deconvoluting a non-uniform detection function from velocity map imaging experiments provided the detection function is measurable independently. Experimentally we demonstrated this technique by recovering the axis distribution of 1D aligned pDIB molecules using laser-induced Coulomb explosion imaging. A major advantage of the technique is that it allows a transferable and complete characterization of the axis distribution of aligned molecules. In particular, $\langle\cos^2\theta\rangle$ can be determined. This represents a measure of the true degree of alignment rather than the usual $\langle\cos^2\Theta_{2D}\rangle$ value, determined directly from 2D ion images, which is strongly biased by the orientational dependence of the probe process. Furthermore, the method also provides higher moments of the axis distribution and as such a complete characterization alignment of the molecules is possible.

V. ACKNOWLEDGEMENTS

We are grateful to Varun Suresh Makhija for helpful discussions on this manuscript.
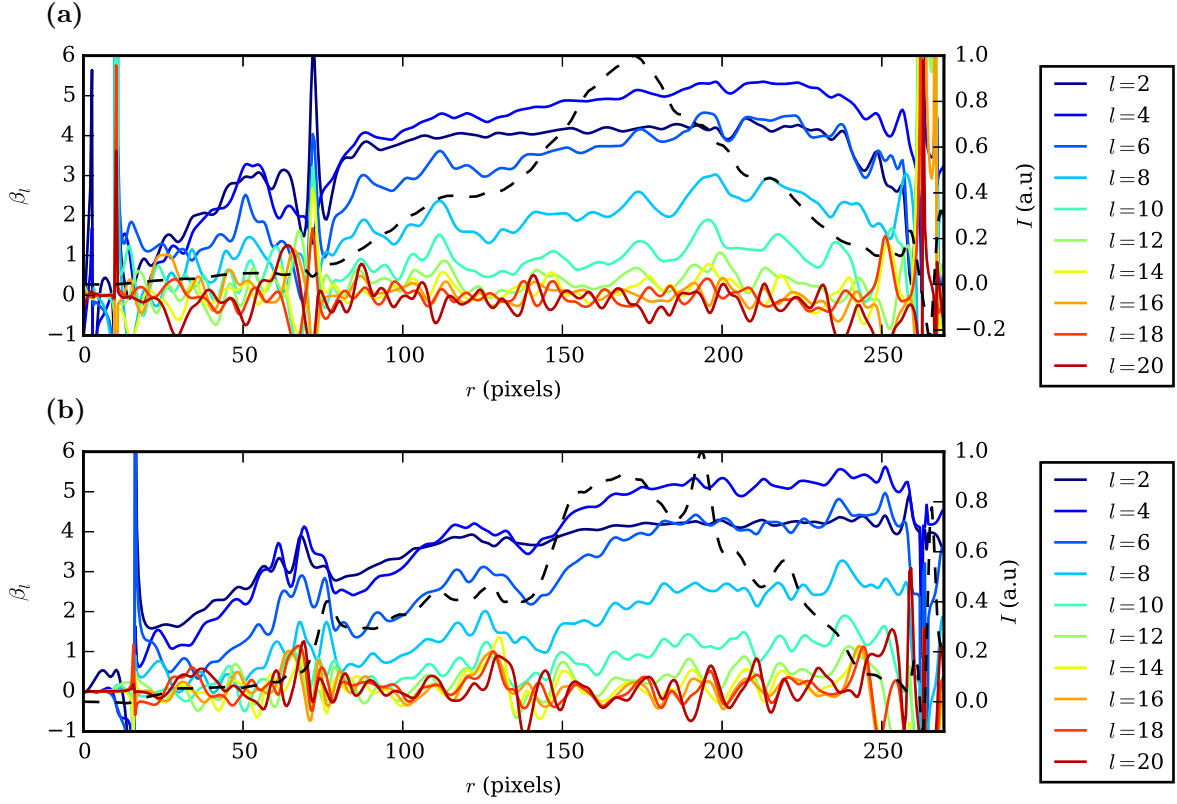
(a)

(b)

FIG. 12. Radial dependence of the $\beta_l(r)$ angular parameters obtained from the deconvoluted pBasex inversion of the images shown in Fig. 8 (solid lines). (a) parallel probe polarization geometry (b) perpendicular probe polarization geometry. The corresponding radial spectra are also shown (dashed lines).

Appendix A: Abel inversion in spherical polar coordinates

For a specific value of r (proportional to the particle velocity), the relationship between the 3D distribution of detected particles, $f(r, \theta, \phi) = g(r, \theta)D(r, \theta, \phi)$, and the observed 2D projected image $F(R, \Theta)$ is

$$F(R, \Theta; r)S_{R\Theta} = f(r, \theta, \phi)S_{\theta\phi} \tag{A1}$$

where $S_{R\Theta}$ is the elementary surface on the detector, and $S_{\theta\phi}$ is the elementary surface on the sphere of radius r,

$$S_{R\Theta} = R\, dR\, d\Theta, \tag{A2}$$

$$S_{\theta\phi} = r^2 \sin\theta\, d\theta\, d\phi. \tag{A3}$$

$S_{R\Theta}$ may be re-written as

$$S_{R\Theta} = R|\mathbf{J}|\, d\theta\, d\phi, \tag{A4}$$

where the determinant of the Jacobian $\mathbf{J}$ is given by

$$|\mathbf{J}| = \left| \frac{\partial R}{\partial \theta} \frac{\partial \Theta}{\partial \phi} - \frac{\partial \Theta}{\partial \theta} \frac{\partial R}{\partial \phi} \right|. \tag{A5}$$

Substituting Eq. (A3), Eq. (A4) and Eq. (A5) into Eq. (A1) we can write

$$F(R, \Theta; r) = \frac{f(r, \theta)r^2 \sin\theta}{R|\mathbf{J}|}. \tag{A6}$$

Noting that

$$R = r\sqrt{\cos^2\theta + \sin^2\theta \sin^2\phi}, \tag{A7a}$$

$$\Theta = \arctan(\sin\phi \tan\theta), \tag{A7b}$$

we can evaluate the Jacobian in Eq. (A5) as

$$|\mathbf{J}| = \left| \frac{2r \sin^2(\theta) \cos(\phi)}{\sqrt{2\cos(2\theta)\cos^2(\phi) - \cos(2\phi) + 3}} \right|. \tag{A8}$$

Using the relationships

$$\phi = \arcsin\left(\frac{\tan\Theta}{\tan\theta} \right), \tag{A9}$$

$$\Theta = \arccos\left(\frac{r\cos\theta}{R} \right), \tag{A10}$$

we can subsitute Eq. (A8) into Eq. (A6) to obtain

$$F(R, \Theta; r) = \frac{r f(r, \theta, \phi)}{\sqrt{r^2 - R^2}}, \tag{A11}$$

with ϕ given by Eq. (A9) and θ given by

$$\theta = \arccos\left(\frac{R\cos\Theta}{r} \right). \tag{A12}$$

Since in general we have more than a single kinetic energy present in the 3D distribution, we have to integrate over $r \geq R$ in order to calculate the projection intensity at (R, Θ):

$$F(R, \Theta) = \int_R^\infty \frac{r f(r, \theta, \phi)}{\sqrt{r^2 - R^2}} \, \mathrm{d}r. \tag{A13}$$

Appendix B: Rotation of the the detection function from the DF to the AF

The detection function in the DF (Eq. (14)) may be re-written as an expansion in spherical harmonics as

$$D(\theta', \phi'; r) = \frac{1}{\sqrt{4\pi}} \sum_{l=0}^{l_{\max}} \sqrt{\frac{4\pi}{2l+1}} \beta_l'(r) Y_{l0}(\theta', \phi'). \tag{B1}$$

The detection function in the AF is related to the detection function in the DF through rotation by the Euler angles (α, Ω, γ).[34] The detection function in the AF can be written as

$$
\begin{aligned}
D(\theta, \phi; r) = \frac{1}{\sqrt{4\pi}} \sum_{l=0}^{l_{\max}} \sqrt{\frac{4\pi}{2l+1}} \beta_l'(r) \\
\times \sum_{m=-l}^{m=l} D_{m0}^l(\alpha, \Omega, \gamma) Y_{lm}(\theta, \phi),
\end{aligned} \tag{B2}
$$

where $D_{mm'}^l(\alpha, \Omega, \gamma)$ are the Wigner rotation matrices. Expressing the rotation matrix $D_{m0}^l(\alpha, \Omega, \gamma)$ in terms of a spherical harmonic yields

$$
\begin{aligned}
D(\theta, \phi; r) = \frac{1}{\sqrt{4\pi}} \sum_{l=0}^{l_{\max}} \frac{4\pi}{2l+1} \beta_l'(r) \\
\times \sum_{m=-l}^{m=l} Y_{lm}^*(\Omega, \alpha) Y_{lm}(\theta, \phi),
\end{aligned} \tag{B3}
$$

The product of two spherical harmonics can be contracted by the spherical harmonic addition theorem,[34]

$$\frac{4\pi}{2l+1} \sum_{m=-l}^{l} Y_{lm}^*(\Omega, \alpha) Y_{lm}(\theta, \phi) = P_l(\cos \Delta), \tag{B4}$$

where Δ is given by Eq. (16). Substitution of Eq. (B4) into Eq. (B3) gives Eq. (15)

Appendix C: Detection function integrated over ϕ

In order to visualize how the detection function samples the axis distribution, it is helpful to calculate the detection function in the AF Eq. (B2) integrated over ϕ. Noting that

$$\int_0^{2\pi} Y_{lm}(\theta, \phi) \, \mathrm{d}\phi = 2\pi \sqrt{\frac{2l+1}{4\pi}} P_l(\cos \theta) \delta_{m0}, \tag{C1}$$

and

$$D_{00}^l(\alpha, \Omega, \gamma) = P_l(\cos \Omega), \tag{C2}$$

we can evaluate the axially integrated detection function as

$$
\begin{aligned}
D(\theta; r) &= \int_0^{2\pi} D(\theta, \phi; r) \, \mathrm{d}\phi \\
&= \sqrt{\pi} \sum_{l=0}^{l_{\max}} \beta_l'(r) P_l(\cos \Omega) P_l(\cos \theta).
\end{aligned} \tag{C3}
$$

Appendix D: Overlap function evaluation

The angular distribution of molecular axes in Eq. (12) can be re-expressed in terms of spherical harmonics as

$$f(\theta; r) = \frac{1}{\sqrt{4\pi}} \sum_l \beta_l \sqrt{\frac{4\pi}{2l+1}} Y_{l0}(\theta, \phi). \tag{D1}$$

Substituting Eq. (B2) and Eq. (D1) into Eq. (17) gives

$$
\begin{aligned}
O(r) = \frac{1}{D_{\max}(r)} \sum_{l=0}^{l_{\max}} \sqrt{\frac{1}{2l+1}} \beta_l(r) \\
\times \sum_{l'=0}^{l'_{\max}} \sqrt{\frac{1}{2l'+1}} \beta_{l'}'(r) \sum_{m'=-l'}^{m'=l'} D_{m'0}^{l'}(\alpha, \Omega, \gamma) \\
\times \int_0^{2\pi} \int_0^\pi Y_{l0}(\theta, \phi) Y_{l'm'}(\theta, \phi) \sin\theta \, \mathrm{d}\theta \, \mathrm{d}\phi,
\end{aligned} \tag{D2}
$$

Evaluating the integral using the orthogonality of spherical harmonics[34] and Eq. (C2) gives

$$O(r) = \frac{1}{D_{\max}(r)} \sum_l \frac{1}{2l+1} \beta_l(r) \beta_l'(r) P_l(\cos \Omega). \tag{D3}$$

[1] B. J. Whitaker, Imaging in Molecular Dynamics: Technology and Applications (Cambridge University Press, 2003).

[2] M. N. Ashfold, N. H. Nahler, A. J. Orr-Ewing, O. P. Vieuxmaire, R. L. Toomes, T. N. Kitsopoulos, I. A. Garcia, D. A. Chestakov, S.-M. Wu, and D. H. Parker, Phys. Chem. Chem. Phys. **8**, 26 (2006).

[3] T. Suzuki, Annu. Rev. Phys. Chem. **57**, 555 (2006).

[4] D. W. Chandler and P. L. Houston, J. Chem. Phys. **87**, 1445 (1987).

[5] A. T. Eppink and D. H. Parker, Rev. Sci. Instrum. **68**, 3477 (1997).

[6] D. Townsend, M. P. Minitti, and A. G. Suits, Rev. Sci. Instrum. **74**, 2530 (2003).

[7] C. Bordas, F. Paulig, H. Helm, and D. Huestis, Rev. Sci. Instrum. **67**, 2257 (1996).

[8] J. Winterhalter, D. Maier, J. Honerkamp, V. Schyja, and H. Helm, J. Chem. Phys. **110**, 11187 (1999).

[9] G. A. Garcia, L. Nahon, and I. Powis, Rev. Sci. Instrum. **75**, 4989 (2004).

[10] B. Dick, Phys. Chem. Chem. Phys. **16**, 570 (2014).

[11] C. Smeenk, L. Arissian, A. Staudte, D. M. Villeneuve, and P. B. Corkum, J. Phys. B: At., Mol. Opt. Phys. **42**, 185402 (2009).

[12]M. Wollenhaupt, M. Krug, J. Khler, T. Bayer, C. Sarpe-Tudoran, and T. Baumert, Appl. Phys. B: Lasers Opt. **95**, 647 (2009).

[13]J. J. Larsen, K. Hald, N. Bjerre, H. Stapelfeldt, and T. Seideman, Phys. Rev. Lett. **85**, 2470 (2000).

[14]F. Rosca-Pruna and M. Vrakking, Phys. Rev. Lett. **87**, 153902 (2001).

[15]P. W. Dooley, I. V. Litvinyuk, K. F. Lee, D. M. Rayner, M. Spanner, D. M. Villeneuve, and P. B. Corkum, Phys. Rev. A **68**, 023406 (2003).

[16]H. Stapelfeldt and T. Seideman, Rev. Mod. Phys. **75**, 543 (2003).

[17]K. F. Lee, D. Villeneuve, P. Corkum, A. Stolow, and J. G. Underwood, Phys. Rev. Lett. **97**, 173001 (2006).

[18]L. Holmegaard, J. H. Nielsen, I. Nevo, H. Stapelfeldt, F. Filsinger, J. Küpper, and G. Meijer, Phys. Rev. Lett. **102**, 023001 (2009).

[19]D. Pentlehner, J. H. Nielsen, A. Slenczka, K. Mølmer, and H. Stapelfeldt, Phys. Rev. Lett. **110**, 093002 (2013).

[20]F. Filsinger, G. Meijer, H. Stapelfeldt, H. N. Chapman, and J. Küpper, Phys. Chem. Chem. Phys. **13**, 2076 (2011).

[21]J. Küpper, S. Stern, L. Holmegaard, F. Filsinger, A. Rouzée, A. Rudenko, P. Johnsson, A. V. Martin, M. Adolph, A. Aquila, S. Bajt, A. Barty, C. Bostedt, J. Bozek, C. Caleman, R. Coffee, N. Coppola, T. Delmas, S. Epp, B. Erk, L. Foucar, T. Gorkhover, L. Gumprecht, A. Hartmann, R. Hartmann, G. Hauser, P. Holl, A. Hömke, N. Kimmel, F. Krasniqi, K.-U. Kühnel, J. Maurer, M. Messerschmidt, R. Moshammer, C. Reich, B. Rudek, R. Santra, I. Schlichting, C. Schmidt, S. Schorb, J. Schulz, H. Soltau, J. C. H. Spence, D. Starodub, L. Strüder, J. Thøgersen, M. J. J. Vrakking, G. Weidenspointner, T. A. White, C. Wunderer, G. Meijer, J. Ullrich, H. Stapelfeldt, D. Rolles, and H. N. Chapman, Phys. Rev. Lett. **112**, 083002 (2014).

[22]J. C. H. Spence and R. B. Doak, Phys. Rev. Lett. **92**, 198102 (2004).

[23]C. J. Hensley, J. Yang, and M. Centurion, Phys. Rev. Lett. **109**, 133202 (2012).

[24]R. J. D. Miller, Annu. Rev. Phys. Chem. **65**, 583 (2014).

[25]J. Itatani, J. Levesque, D. Zeidler, H. Niikura, H. Ppin, J.-C. Kieffer, P. B. Corkum, and D. M. Villeneuve, Nature **432**, 867 (2004).

[26]R. Torres, N. Kajumba, J. G. Underwood, J. Robinson, S. Baker, J. Tisch, R. De Nalda, W. Bryan, R. Velotta, C. Altucci, et al., Phys. Rev. Lett. **98**, 203007 (2007).

[27]V. Kumarappan, L. Holmegaard, C. Martiny, C. B. Madsen, T. K. Kjeldsen, S. S. Viftrup, L. B. Madsen, and H. Stapelfeldt, Phys. Rev. Lett. **100**, 093006 (2008).

[28]P. Hockett, C. Z. Bisgaard, O. J. Clarkin, and A. Stolow, Nature Phys. **7**, 612 (2009).

[29]R. Boll, D. Anielski, C. Bostedt, J. Bozek, L. Christensen, R. Coffee, S. De, P. Decleva, S. Epp, B. Erk, L. Foucar, F. Kras-niqi, J. Küpper, A. Rouze, B. Rudek, A. Rudenko, S. Schorb, H. Stapelfeldt, M. Stener, S. Stern, S. Techert, S. Trippel, M. J. J. Vrakking, J. Ullrich, and D. Rolles, Phys. Rev. A **88**, 061402(R) (2013).

[30]M. J. J. Vrakking, Rev. Sci. Instrumen. **72**, 4084 (2001).

[31]G. M. Roberts, J. L. Nixon, J. Lecointre, E. Wrede, and J. R. R. Verlet, Rev. Sci. Instrumen. **80**, 053104 (2009).

[32]However we note that the methodology presented here can be applied to other choices of coordinate frames and our early work on this resulted in a treatment using cartesian coordinates which unfortunately resulted in amplification of experimental noise[48].

[33]M. Galassi, J. Davies, J. Theiler, B. Gough, G. Jungman, M. Booth, and F. Rossi, Gnu Scientific Library: Reference Manual (Network Theory Ltd., 2003).

[34]R. N. Zare, Angular Momentum: Understanding spatial aspects in chemistry a (John Wiley & Sons, 1988).

[35]J. G. Underwood, B. J. Sussman, and A. Stolow, Phys. Rev. Lett. **94**, 223001 (2005).

[36]V. Kumarappan, C. Z. Bisgaard, S. S. Viftrup, L. Holmegaard, and H. Stapelfeldt, J. Chem. Phys. **125**, 194309 (2006).

[37]B. Friedrich and D. Herschbach, J. Phys. Chem. **99**, 15686 (1995).

[38]L. Christiansen, D. Pentlehner, J. H. Nielsen, J. G. Underwood, and H. Stapelfeldt, "Alignment enhancement of molecules embedded in helium nanodroplets by multiple laser pulses," (2015), submitted for publication.

[39]M. Bertero and P. Boccaci, Introduction to inverse problems in imaging (IOP, 1998).

[40]F. Renth, J. Riedel, and F. Temps, Rev. Sci. Instrumen. **77**, 033103 (2006).

[41]X. Xie, K. Doblhoff-Dier, H. Xu, S. Roither, M. S. Schöffler, D. Kartashov, S. Erattupuzha, T. Rathje, G. G. Paulus, K. Yamanouchi, A. Baltuška, S. Gräfe, and M. Kitzler, Phys. Rev. Lett. **112**, 163003 (2014).

[42]T. Seideman, M. Y. Ivanov, and P. B. Corkum, Phys. Rev. Lett. **75**, 2819 (1995).

[43]C. Ellert and P. B. Corkum, Phys. Rev. A **59**, R3170 (1999).

[44]J. L. Hansen, L. Holmegaard, J. H. Nielsen, H. Stapelfeldt, D. Dimitrovski, and L. B. Madsen, J. Phys. B: At., Mol. Opt. Phys. **45**, 015101 (2012).

[45]T. K. Kjeldsen, C. Z. Bisgaard, L. B. Madsen, and H. Stapelfeldt, Phys. Rev. A **71**, 013418 (2005).

[46]I. V. Litvinyuk, K. F. Lee, P. W. Dooley, D. M. Rayner, D. M. Villeneuve, and P. B. Corkum, Phys. Rev. Lett. **90**, 233003 (2003).

[47]D. Pavičić, K. F. Lee, D. M. Rayner, P. B. Corkum, and D. M. Villeneuve, Phys. Rev. Lett. **98**, 243001 (2007).

[48]I. Procino, Laser induced molecular axis alignment: measurement and applica Ph.D. thesis, University College London, Department of Physics and Astronomy, University College London, Gower Street, London WC1E 6BT, UK (2011).